

Temporal Evolution of Photon Energy emitted from Two Component Advective Flows: Origin of Time Lag

Arka Chatterjee^{1*}, Sandip K. Chakrabarti^{2,1†} and Himadri Ghosh^{‡3,1}

¹Indian Centre for Space Physics, Chalantika 43, Garia Station Rd., Kolkata, 700084, India

²S. N. Bose National Centre for Basic Sciences, Salt Lake, Kolkata, 700098, India

³Heritage Institute of Technology, Kolkata, 700107, India

Accepted XXX. Received YYY; in original form ZZZ

ABSTRACT

X-Ray time lag of black hole candidates contains important information regarding the emission geometry. Recently, study of time lags from observational data revealed very intriguing properties. To investigate the real cause of this lag behavior with energy and spectral states, we study photon paths inside a Two Component Advective Flow (TCAF) which appears to be a satisfactory model to explain the spectral and timing properties. We employ the Monte-Carlo simulation technique to carry out the Comptonization process. We use a relativistic thick disk in Schwarzschild geometry as the CENTrifugal pressure supported BOundary Layer (CENBOL) which is the Compton cloud. In TCAF, this is the post-shock region of the advective component. Keplerian disk on the equatorial plane which is truncated at the inner edge i.e., at the outer boundary of the CENBOL, acts as the soft photon source. Ray-tracing code is employed to track the photons to a distantly located observer. We compute the cumulative time taken by a photon during Comptonization, reflection and following the curved geometry on the way to the observer. Time lags between various hard and soft bands have been calculated. We study the variation of time lags with accretion rates, CENBOL size and inclination angle. Time lags for different energy channels are plotted for different inclination angles. The general trend of variation of time lag with QPO frequency and energy as observed in satellite data is reproduced.

Key words: black hole physics – accretion, accretion discs – radiative transfer – X-ray time lags

1 INTRODUCTION

Many of the X-ray sources studied by UHURU, Ginga, Rossi X-ray Timing Explorer (RXTE) Monitor of All-sky X-ray Image (MAXI), NuSTAR and ASTROSAT are Black Hole Candidates (BHCs). The behavior of the spectral and timing properties across the time scales are of great interest to understand the geometry of the emitting gas. The spectrum mostly consists of a multi-color black-body component at around 0.1 – 5 keV and a power-law component which may go up to hundreds of keV often having an exponential cut-off. The study of the evolution in the spectral state is considered to be the most promising way to learn about the intrinsic properties such as the mass M and spin a of black hole candidates and as well as the properties and dynamics of the flow accreting onto it. There are several models in

the literature which attempt to understand these properties. Basically all the models start with the standard Shakura-Sunyaev (1973) Keplerian disk along with a hot electron cloud located nearby (Takahara, Tsuruta & Ichimaru, 1981; Maraschi, Roasio & Treves, 1982; Sunyaev & Titarchuk, 1989; Haardt & Maraschi, 1991,1993). In the present paper, we concentrate on the Two Component Advective Flow (hereafter TCAF) solution (Chakrabarti & Titarchuk 1995, hereafter CT95) whose every feature is derived from fundamental equations which govern the flow (Chakrabarti, 1990; 1996). This solution directly derives the physical flow parameters by fitting the data with a minimal set of parameters (see, Debnath et al. 2014; Mondal et al. 2014; Jana et al. 2015; Molla et al. 2016; Chatterjee et al. 2016) instead of just dwelling on the extrinsic and derivable properties such as the fluxes, spectral slopes and hard or softness as used in other models. The parameters required for TCAF fit of any spectrum are the accretion rates (halo rate \dot{m}_h and disk rate \dot{m}_d), the shock location X_s (which represents the size of Compton cloud) and the strength of shock R (defined as

* E-mail: arka@csp.res.in

† E-mail: chakraba@bose.res.in

‡ himadri.ghosh@heritageit.edu

the ratio of post-shock (ρ_+) and pre-shock density (ρ_-) and of course the mass of the black hole M .

For a set of flow parameters, TCAF provides the spectrum consisting of the multi-color black body and power-law components with possible reflection and cut-offs combined. However, the photons at the observers frame arrive after various physical processes, such as multiple scattering in the Compton cloud (i.e., the CENtrifugal pressure supported BOundary Layer or CENBOL in TCAF paradigm), reflections, focussing effects apart from the normal changes in time-delay due to space-time curvature at the emission region. Thus, hard and soft photons need not arrive simultaneously. The difference of time between the hard H_t and the soft S_t photons is called lag t_{lag} .

$$t_{lag} = H_t - S_t. \quad (1)$$

If t_{lag} is positive, it is called the hard lag and the opposite is true for the soft lag. The time lag is calculated by averaging the time of arrival of all photons for a given energy band. The observational confirmation of such hard and soft lags are regularly reported in the literature (e.g., Miyamoto et al. 1988; Cui et al. 2000; Qu et al. 2010; Uttley et al. 2011; Dutta & Chakrabarti, 2016). These lags are mostly studied for Low Frequency QPOs of Galactic black holes and perturbations in AGNs and Quasars. In this paper, we concentrate on Galactic black holes. It is believed that Comptonization plays a major role in the lag properties of Galactic black holes (Payne 1980). Numerous models (e.g., Cui et al. 1999; Nowak et al. 1999; Poutanen 2001) have been proposed to explain the lag properties. Ohkawa et al. (2005) explained the lag behavior of GRS 1915+105 using Comptonization model. However, no unique photon emitting system which decides the lag behavior is theoretically established. Dutta & Chakrabarti (2016, hereafter DC16) provided a list of contributors (e.g., Comptonization, disk reflection and gravitational lensing) to the time lag and the possible outcome, attempting for the first time to explain difference in behavior of systems with both low and high inclination angles. Our present simulation is to actually reproduce magnitudes of these contributions and see if any new effects are important. Compton upscattering naturally produces the hard lag. The connection with oscillation of Comptonization region to QPO frequency has already been established by Chakrabarti & Manickam (2000, CM00) after extending the results of the numerical simulations of the oscillatory shocks in advective flows by Molteni, Sponholz & Chakrabarti (1996) (hereafter MSC96). So, the lag variation with QPO frequency or shock location X_s is the natural outcome of TCAF solution. Lags are generally produced due to the light crossing time through different regions of the accretion disk and thus the main challenge is to find out how the path lengths of the observed photons vary with their energies.

Spectral variabilities with inclination angle is observed and reported several times in the literature (e.g., Motta et al. 2015; Heil et al. 2015). Since it is impossible for us to observe a particular BHC in different inclination angles, we must carry out the Monte-Carlo simulation of a realistic system to check if the lag properties are generally different from various angles as observed. Using the same procedure, earlier Ghosh et al. (2011) established that the spectrum becomes harder if observed at a high inclination angle. However, that was purely due to projection effects. Chatterjee,

Chakrabarti & Ghosh (2017, hereafter CCG217) performed ray-tracing of the photons emitted by a Monte-Carlo method and projected them on the observer plane. They showed that the image and the spectra both change with the inclination angle as the contribution of hard photons increases. This motivates us to study the variation of time lag with various flow parameters, such as, the accretion rate, CENBOL size (shock location), photon energy, theoretically calculated QPO frequency from the shock location and, of course, the inclination angle.

In this paper, we present simulated results of time lags found in the phasor part of the Power Density Spectrum (PDS) of BHCs using TCAF geometry. In the next Section, we describe the geometry and thermodynamical properties of TCAF used in the simulation. In §3, we briefly describe the ray-tracing mechanism. Section 4 describes the Monte-Carlo simulation process. We then present our results in Sec 5. This is followed by Discussions and Conclusions.

2 GEOMETRY OF THE PROBLEM

TCAF mainly consists of a Keplerian flow with higher angular momentum and an advective, sub-Keplerian component with low angular momentum surrounding the Keplerian disk. Sub-Keplerian flow or the halo component puffs up after reaching the centrifugal barrier known as the Shock Location (X_s). Depending on the criteria for a shock to form, i.e., whether the Rankine-Hugoniot conditions are satisfied or not, the shock may be stationary (Landau & Lifshitz, 1959) or oscillating depending upon the geometry and the thermodynamical properties of flow parameters. In Molteni et al. (1994), it was pointed out that the post-shock region or CENBOL behaves like thick disks as envisaged by Abramowicz et al., 1978; Kozłowski et al., 1978; Paczyński & Wiita, 1980; Begelman, Blandford & Rees, 1982; Chakrabarti, 1985; hereafter C85) though the simulation results are more accurate due to the presence of radial velocity. In the present paper, we consider C85 prescription to obtain relativistic thick disk parameters in our geometry. This hot region acts as the Compton cloud where soft photons from the Keplerian disk are intercepted and inverse-Comptonized to create a power-law tail as theoretically calculated in CT95. Below, we briefly describe the geometry and thermodynamical properties of the CENBOL and the Keplerian disk. We consider the natural units where $r_g = \frac{2GM}{c^2} = 2$ with $G = 1$, $M = 1$ and $c = 1$ throughout the paper. Accretion rate is measured in Eddington unit, i.e., $\dot{m}_d = \frac{\dot{M}}{M_{Edd}}$. In this work, we considered the outer edge of truncated Keplerian disk to be extended up to $100r_g$. CENBOL size varies from $20r_g$ to $65r_g$. Outer edge of CENBOL is the inner edge of the Keplerian disk.

2.1 Compton Cloud or CENBOL

Euler's equation for a perfect fluid can be written as,

$$\frac{\nabla p}{p + \epsilon} = -\ln(u_t) + \frac{\Omega \nabla l}{(1 - \Omega)} \quad (2)$$

(for details, see, C85). Also, $l = -u_\phi/u_t$ is the specific angular momentum and $\Omega = u^\phi/u^t$ is the relativistic angular

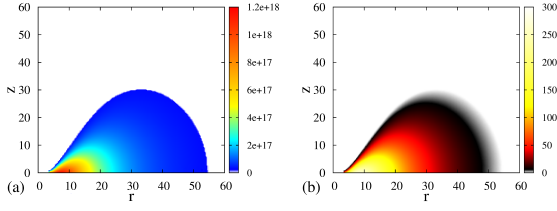


Figure 1. Typical (a) electron number density (in per cm^3) and (b) temperature (in keV) distributions are shown. The central region of CENBOL contains the maximum density and temperature.

velocity. Four velocity is considered as $[u_t, 0, 0, u_\phi]$. To enforce equipotential surfaces to remain the same as the equipressure surface, we choose the barotropic ($p(\epsilon)$) equation of state. So, Euler's equation becomes,

$$W - W_{in} = \int_0^p \frac{dp}{p + \epsilon} = \int_{u_t}^{u_t} \ln(u_t) - \int_{l_{in}}^l \frac{\Omega \nabla l}{(1 - \Omega l)}, \quad (3)$$

where, the natural angular momentum distribution ($l = c\lambda^n$, c and n are constants) yields the von-Zeipel relation $\Omega = \Omega(l) = c^{2/n} l^{1-2/n}$ with $\lambda = \frac{r \sin \theta}{(1 - \frac{r}{r_c})^{1/2}}$ (C85, Paper1). Since, by definition, the angular momentum distribution of a thick disk intercepts the Keplerian distribution at two points, namely, the inner boundary (r_{in}) and the centre of disk (r_c), it is easy to calculate the values of c and n using algebraic equations from those points (C85). Once, we fix the constants of the flow, the equipotential surfaces filled with matter creates the CENBOL region. In reality, density drop near the outer edge is faster than what is chosen here. This is due to the presence of a shock front. The gradual drop of density at the outer edge of the CENBOL which we have chosen here would correspond to the presence of a weaker shock.

For Comptonization, we need to provide the exact number density and temperature of electron in each grid of the CENBOL region. We use polytropic equation of state, $p = K\rho^\gamma$, where p is pressure, ρ is the matter density, K is the constant or measure of entropy of the system and γ is the polytropic index. Value of γ is considered to be $4/3$. Typical electron number density and temperature is shown in Figure 1.

2.2 Keplerian disk as the Soft Photon Source

Keplerian disk is situated outside the Compton cloud boundary or the shock location X_s on the equatorial plane. Theoretically, it has a higher viscosity (see, Chakrabarti 1990; Chakrabarti 1996; Chakrabarti & Das 2004 and Nagarkoti & Chakrabarti 2016) and much lower temperature than the CENBOL region. Thermal photons are produced in the Keplerian disk via black body emission. The truncated Keplerian disk extends up to $100 r_g$. Radiation profile of Keplerian disk adopted from Page & Thorne, (1974). Inner edge of the

Keplerian disk and outer edge of the CENBOL coincides. Flux and temperature profiles are given below.

$$F(r) = \frac{F_c(\dot{m}_d)}{(r-3)r^{5/2}} \times \left[\sqrt{r} - \sqrt{6} + \frac{\sqrt{3}}{3} \log \left(\frac{(\sqrt{r} + \sqrt{3})(\sqrt{6} - \sqrt{3})}{(\sqrt{r} - \sqrt{3})(\sqrt{6} + \sqrt{3})} \right) \right] \quad (4)$$

and

$$T(r) = \left(\frac{F(r)}{\sigma} \right)^{1/4}$$

where, $F_c(\dot{m}_d) = \frac{3m\dot{m}_d}{8\pi r_g^3}$, with \dot{m}_d being the disk accretion rate in Eddington unit, $\sigma = \frac{2\pi^5 k^4}{15h^3 c^3}$ is the Stefan-Boltzmann constant.

Photon flux emitted from the Keplerian disk surface having radius r to $r + \delta r$ is given by,

$$n_\gamma(r) = \left[\frac{4\pi}{c^2} \left(\frac{k_b T(r)}{h} \right)^3 \times \zeta(3) \right] cm^{-2} s^{-1}, \quad (5)$$

where, $\zeta(3) = \sum_{l=1}^{\infty} l^{-3} = 1.202$ is the Riemann zeta function. The rate of photons emitted Keplerian disk having radius r to $r + \delta r$ is given by

$$dN(r) = 4\pi r \delta r n_\gamma(r) s^{-1}, \quad (6)$$

(see, Garain, Ghosh & Chakrabarti, 2014, for further details).

For the sake of simulations of photon injection to CENBOL, the Keplerian disk is divided into several annuli of width $D(r) = 0.1$. $T(r)$ is the temperature of the mean radius of each annulus. The total number of photons turn out to be $\sim 10^{39} - 10^{40}$ per second for $\dot{m}_d = 0.1$. To save computational time, we bundle photons using a weightage factor $f_W = \frac{dN(r)}{N_{comp}(r)}$ where $N_{comp}(r) = 10^8$.

We calculate soft photon energy using Planck distribution law for $T(r)$. The number density of photons ($n_\gamma(E)$) which correspond to an energy E is given by,

$$n_\gamma(E) = \frac{1}{2\zeta(3)} b^3 E^2 (e^{bE} - 1)^{-1}, \quad (7)$$

where, $b = 1/kT_k^{disk}(r)$ (e.g., Ghosh, Chakrabarti, Laurent, 2009, hereafter GCL09).

3 RAY TRACING PROCESS

The ray-tracing equations are derived from field equation using non-vanishing Christoffel terms in Schwarzschild geometry,

$$\frac{d^2 x^\mu}{dp^2} + \Gamma_{\nu\lambda}^\mu \frac{dx^\nu}{dp} \frac{dx^\lambda}{dp} = 0, \quad (8)$$

where, $\mu = [0, 1, 2, 3]$; $x^0 = t$, $x^1 = r$, $x^2 = \theta$ and $x^3 = \phi$, p is the affine parameter. We obtain four coupled, second order differential equations for photons where 4-momentum $P_t = E = (1 - \frac{2}{r}) \frac{dt}{dp}$ and $P_\phi = L = r^2 \sin^2 \theta \frac{d\phi}{dp}$ definitions are used (Chandrasekhar, 1983) to shift the base from an affine parameter p to time t . Thus, we retain three equations in

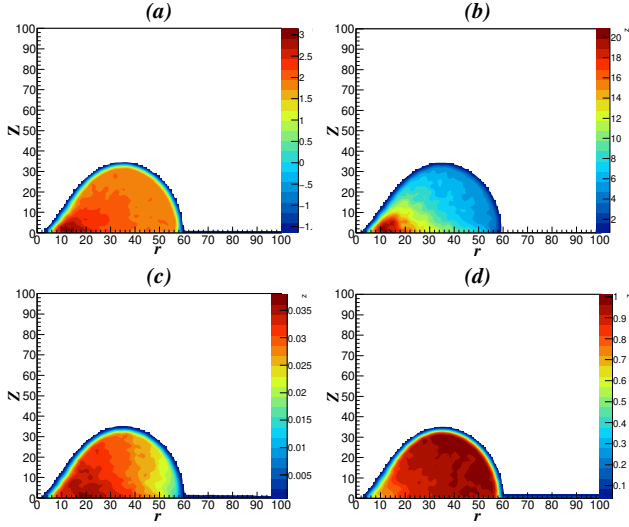


Figure 2. (a) Energy (in keV plotted in log scale) of escaping Photons, (b) number of scattering (dimensionless number) suffered by emergent photons from the CENBOL, (c) contours of constant time (in sec) of emission of photons after Comptonization and (d) vertical component of velocity of photons (in the unit of velocity of light) are represented for a CENBOL which has the outer edge at around $60r_g$.

3D geometry with time as the base.

$$\begin{aligned} \frac{d^2 r}{dt^2} + \frac{3}{r(r-2)} \left(\frac{dr}{dt} \right)^2 - (r-2) \left(\frac{d\theta}{dt} \right)^2 - \\ (r-2) r \sin^2 \theta \left(\frac{d\phi}{dt} \right)^2 + \frac{r-2}{r^3} = 0, \quad (9) \\ \frac{d^2 \theta}{dt^2} + \frac{2r-6}{r(r-2)} \left(\frac{d\theta}{dt} \right) \left(\frac{dr}{dt} \right) - \sin \theta \cos \theta \left(\frac{d\phi}{dt} \right)^2 = 0 \text{ and} \\ \frac{d^2 \phi}{dt^2} + \frac{2r-6}{r(r-2)} \left(\frac{d\theta}{dt} \right) \left(\frac{dr}{dt} \right) + 2 \cot \theta \left(\frac{d\theta}{dt} \right) \left(\frac{d\phi}{dt} \right) = 0. \end{aligned}$$

Velocity components are derived from the transformation equations (Park, 2006) and written as,

$$\begin{aligned} v^{\hat{r}} = \frac{d\hat{r}}{dt} = \frac{r}{(r-2)} \frac{dr}{dt}, \quad v^{\hat{\theta}} = \frac{d\hat{\theta}}{dt} = \frac{r\sqrt{r}}{\sqrt{(r-2)}} \frac{d\theta}{dt} \\ \text{and } v^{\hat{\phi}} = \frac{d\hat{\phi}}{dt} = \frac{r\sqrt{r}\sin\theta}{\sqrt{(r-2)}} \frac{d\theta}{dt}. \quad (10) \end{aligned}$$

The process of Ray-Tracing is similar to CCG17.

4 MONTE-CARLO COMPTONIZATION

Using straight line path of photons between two successive scatterings inside the Compton cloud saves some computational time without any loss of physics (Laurent & Titarchuk, 1999). The injected photons are generated from the Keplerian disk at a random direction which required use of three random numbers. In the Monte-Carlo simulation, the functional form of $\cos\theta$ for the flux dependence of photons on θ is implemented as is the case where temperature gradient inside the Keplerian disk is along Z axis. Inside the CENBOL, a critical optical depth τ_c is set up from a random number after each scattering. When the traversed

optical depth of a given photon crosses τ_c , it is allowed to make the next scattering.

The Klein-Nishina scattering cross section σ is given by:

$$\sigma = \frac{2\pi r_e^2}{x} \left[\left(1 - \frac{4}{x} - \frac{8}{x^2} \right) \ln(1+x) + \frac{1}{2} + \frac{8}{x} - \frac{1}{2(1+x)^2} \right], \quad (11)$$

where, x is given by,

$$x = \frac{2E}{mc^2} \gamma \left(1 - \mu \frac{v}{c} \right), \quad (12)$$

$r_e = e^2/mc^2$ is the classical electron radius and m is the mass of the electron.

The energy exchange via Comptonization or inverse Comptonization is calculated in each step assuming an electron with randomly chosen momentum vectors. While travelling from one scattering centre to another, the gravitational redshift acts on a photon changing its frequency. The process continues until the photon leaves CENBOL region or is sucked in by the black hole. The process is similar to what was used in GCL09; Ghosh, Garain, Chakrabarti, Laurent, 2010; Ghosh et al. 2011 (hereafter GGGC11); CCG17.

Figure 2 is the outcome of our Monte-Carlo simulated Comptonization code. The last scattering point of photons are stored. The energy contours (in Panel a) shows the most energetic photons came from the central region where they suffered most scatterings. Panel (b) shows the color gradient map of number of scatterings suffered by individual photons. Contours of constant time of emission are represented in Panel (c). The more time a photon spends inside the CENBOL the more scattering it suffers. Panel (d) shows the magnitude of velocity along the z-axis. It is to be noted that the azimuthal component of velocity (v_z) is nearly unity in upper side of CENBOL. This means the photons from this region will go along the z-axis.

5 RESULTS

The results shown here assume the mass of the black hole to be 10 solar mass.

5.1 Spectra

We used Monte-Carlo method to simulate Comptonization inside the CENBOL region. Figure 3a shows the injected soft photon spectrum. Composite emission spectra for disk and scattered Comptonized photons with the variation of CENBOL size are shown in Fig. 3b. The hardest spectrum corresponds to the largest CENBOL region. The black-body peak of the spectra shifts in lower energy range with the increasing CENBOL size since the inner edge of the Keplerian disk recedes from the black hole.

These results agree with the spectral shape discussed in CT95 and Chakrabarti (1997). Fig. 3(c-d) represent the same spectra for the lowest ($0^\circ - 9^\circ$) and the highest ($81^\circ - 90^\circ$) inclinations respectively. The hardness of the source spectrum over the inclination angle is profoundly visible in these two panels. Detailed information on inclination dependent spectra was provided in Ghosh et al. (2011) and CCG2017.

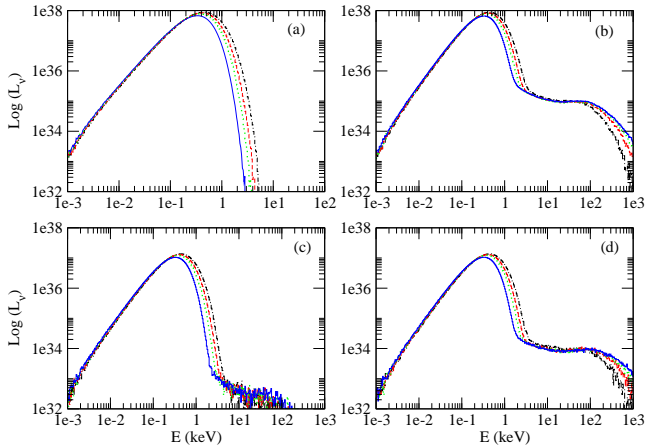


Figure 3. Spectral variation with the outer edge of CENBOL located at $20r_g$ (solid-black), $30r_g$ (dash-dash-dot-red), $40r_g$ (dashed-green) & $65r_g$ (dot-dot-dash-blue). (a) the injected spectra, (b) Emergent Comptonized spectra for photons emitted in all directions, (c) spectra as seen from nearly along the Z-axis and

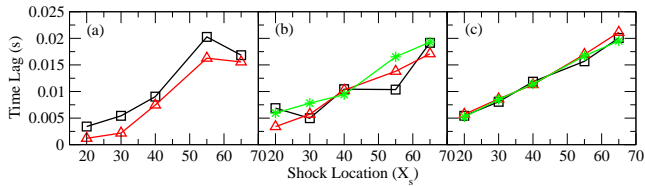


Figure 4. Time lag (*in sec*) between hard band (5–100) keV and soft band (0.1–5) keV is plotted against Shock Location (X_s). (a) Black (square) and red (triangle) lines represent 0° & 10° , (b) Black (square), red (triangle) & green (star) lines represents 20° , 36° & 50° respectively and (c) Black (square), red (triangle) & green (star) lines represent 60° , 70° & 80° respectively.

5.2 Time lag with CENBOL size

It has been reported in DC16 that the time lag increases with the increasing of the CENBOL size i.e., the shock location X_s .

Following this, we simulate cases with variable CENBOL size. The hard band is considered 5 to 100 keV and soft band is considered as 0.1 to 5 keV as in XMM satellite. From our simulations, we see that the time lag actually increases with the shock location. Figure 4 is plotted for three different bins of inclination angle: (a) low inclination (0° & 10°), (b) mid range inclination (20° , 36° & 50°) and (c) for high inclination angles (60° , 70° & 80°). For panel (c), we see the monotonical increase of time lag w.r.t CENBOL size. This region is mostly dominated by the lensing and disk reflection. Hard photons that have generated well inside the Compton cloud takes time to come out. Note that the time lag we obtained is slightly smaller than generally observed values. This is because we use small CENBOL sizes to save computational time. Further details are provided in Sec. 5.5.

5.3 Time Lag with accretion rate

We study accretion rate variation for a fixed CENBOL size to see how it affects the lag features. The results are plot-

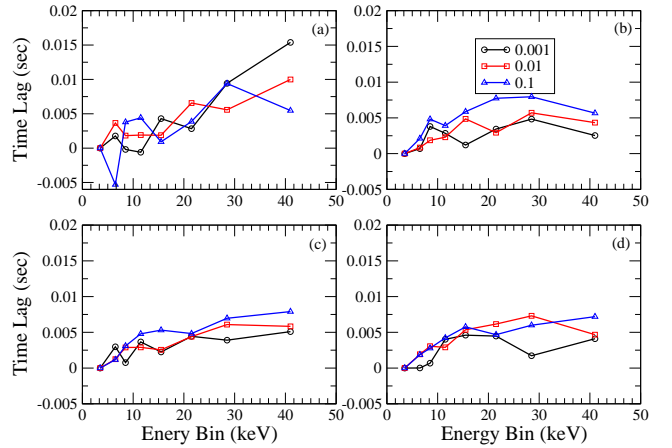


Figure 5. Time lag w.r.t 2.0–5.0 keV plotted for three accretion rates (marked) as a function of observed energy at 0° , 36° , 60° & 80° inclination angles in (a), (b), (c) & (d) respectively. CENBOL size is kept fixed at $65r_g$.

ted in Fig. 5 for four different inclination angles. Accretion rates of the Keplerian component are written in each panel. Apart from very low inclination angle we did not see any soft lag. We see the marginal trend of higher accretion rate causing higher hard lag. From CT95, it is known that higher \dot{m}_d causes softer spectrum for a given sub-Keplerian Component rate (which, together with the Keplerian rate, determines the CENBOL optical depth). The soft photons intercepted by the Compton cloud spends more time and are more energized by CENBOL. So, the value of hard lag increases in for higher energy bins. This is the contribution of Comptonization to the lag feature.

The change in t_{lag} for each energy bin for different \dot{m}_d fluctuates. However, the lag magnitude generally decreases with the inclination angle. Soft lag in Fig. 5(a) is found for accretion rate 0.1 where the observer is face on with the disk. From Panel (d) of Fig. 2, we get the idea of vertical velocity distribution of photons. The top of the CENBOL contains photons having $v_z = 1$. Those reach the observer earlier than the soft photons from Keplerian disk. Since they have scattered from the outer edge of the CENBOL, they are much likely to be ≤ 10 keV. They will contribute to the soft lag for low inclination angle sources. It is to be noted that to understand the complete variation of time lag with accretion rate one needs to supply two types of accretion rates (halo rate (\dot{m}_h) and disk rate (\dot{m}_d) (CT95). The hydrodynamical simulations using two accretion rates are out of the scope of this paper and will be reported elsewhere.

5.4 Variation of Lag with Energy of Photon

For Galactic black hole candidates, Comptonization is an essential component to produce the hard photons. Mostly, inverse Comptonization in the CENBOL region generates the harder photons. Most energetic photons are ejected from the central region (Fig. 2a) of CENBOL where electron density and temperature are maximum. Those photons suffer maximum number of scatterings as depicted in Fig. 2b. The more time photons spend inside the CENBOL the probability of hardening becomes higher. So, Comptonization in general

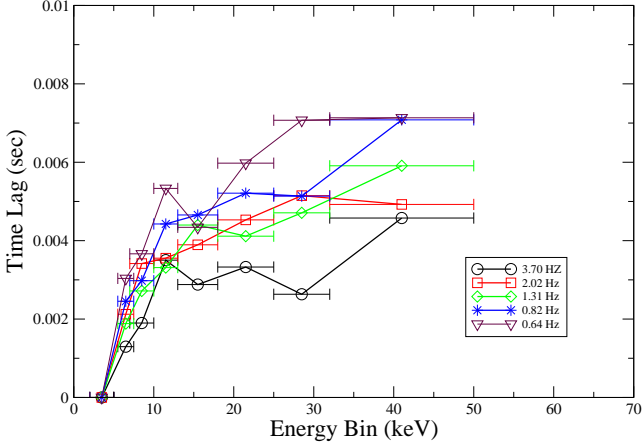


Figure 6. Time lag w.r.t. 2.0 – 5.0 keV is plotted for various energy bins at a range of theoretically obtained QPO frequencies for a fixed inclination angle of 70° .

provides hard lag which can be seen in Fig. 6. From Fig. 6, we find that the lag increases with decreasing QPO frequency. These QPO frequencies are theoretically obtained from the relation provided by CM00 and is given by

$$\nu_{qpo} = \frac{C}{RX_s(X_s - 1)^{1/2}} \sim \frac{C}{RX_s^{3/2}}, \quad (13)$$

where, C is a constant. R & X_s are compression ratio and shock location respectively. MSC96 has showed that the time period of QPO oscillation is comparable with the infall timescale of the postshock region ($t_{infall} \propto X_s^{3/2}$). Thus, the QPO frequency will be inversely proportional to $X_s^{3/2}$. This relation has predicted QPO frequencies for GRS 1915+105 (CM00) and for many other sources (Debnath, Chakrabarti & Mondal, 2014). Observational evidence of such lag behavior is given in DC16. The lag magnitude is somewhat lesser than what people had observed (Nowak et al. 1999; DC16 and Misra et al. 2017). This could be because of the smaller size of the accretion disk and Compton cloud we have considered for our simulation. To reduce computational time, we have restricted ourselves within $100r_g$ of the Standard disk. Bigger CENBOL size ($\sim 500r_g$) would provide an energy dependent lag up to 0.03 Sec. A general trend of dipping in the curve can be seen at 13 – 17 keV energy band in Fig. 6. These are the photons which suffered more scatterings, but, from the outer layer of CENBOL than that by the photons in 7 – 13 keV energy band. So, they arrive a little earlier.

5.5 Variation of Lag with inclination angle

In our previous studies (Chatterjee & Chakrabarti 2015a, 2015b), we have considered only lensing effect by using pure Keplerian disk. There, we have shown the time of arrival changes drastically with increasing inclination angles. Fig. 7 is a time of arrival map of Keplerian disk. For 0° case, photons from inner region of the disk come earlier than the outer region. But, the secondary photons (those which encircle the black hole once or more) originated from various locations of disk may take much longer time of arrival as depicted in Fig. 7a (points beyond 80 in the z-range). At

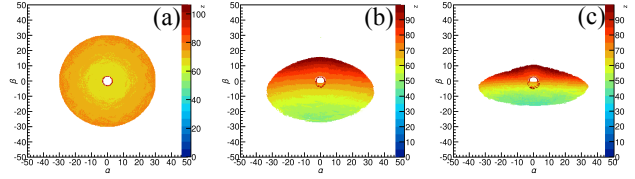


Figure 7. Time of arrival (in r_g/c unit) of photons are mapped on top the images Keplerian disk geometry only. Colorbar represents the time of arrival to a distant observer. Inclinations angles of the observer are 0° , 50° & 70° in panels (a), (b) & (c) respectively. Note the upper band of the color-bar where all the secondary photons have arrived much later than the primary photons. All secondary photons are considered to produce this image.

50° , the same disk looks different. Time of arrival of photons drastically changes at 70° . Light crossing time splits two sides of the Keplerian disk. The secondary photons take even more time to reach the observer frame as the observer moves to higher inclination angles. Here, the inner boundary of Keplerian disk is at $6r_g$ while the outer boundary is at $30r_g$. The position of the observer on azimuthal plane is at 45° . From this Figure, one can easily estimate the light crossing time for much larger accretion disks and for various observer inclinations. For the purpose of observational data, we have added Comptonization and disk reflection into the study. After addition, the composite nature of time lag with the variation of inclination angle has been depicted.

DC16 explained the hard and soft lag features using XTE J1550-564 ($\sim 75^\circ$ inclination) and GX 339-4 ($\sim 50^\circ$ inclination). The processes that take part in the time lag are Comptonization, disk reflection and gravitational lensing. In Fig. 8, we show the lag behavior of 5 – 7 keV and 25 – 30 keV band photons with increasing CENBOL size. The separation between these two lags increases with increasing CENBOL size. Photons generated via inverse Compton scattering can come out from any optical depth of the Compton cloud (see, Fig. 2 and CCG17 for image description). Relatively low energy photons, such as 5 – 7 keV bin are mostly produced from the outer layer of CENBOL and 25 – 30 keV or even higher energy photons come from inner regions. So, with increasing size of CENBOL the distance between outer layer and central region increases and time taken by a harder photon increases.

In Fig. 8, we see the lag variation of 5 – 7 keV photons in first three panels. In panel (d), for 80° inclination angle, the lag variation with respect to CENBOL size for 5 – 7 keV is negligible. This is due to the predominant edge view of CENBOL from that angle. Keplerian disk is extended at the edge of Compton cloud. Soft photons from Keplerian disk participate in the reference energy band of 2 – 5 keV. So, the lag between the reference band and 5 – 7 keV band still remains almost constant for variable Compton cloud in this near edge on scenario. It is to be noted that, for Fig. 4c, the hard energy band is taken from 5-100 keV. For Fig. 8d, the energy bands are splitted (5-7, 7-10, 10-13, 13-18, 18-25 keV etc.). Fig. 8 as a whole is meant to show the lag properties of each separate bands. We can see the monotonic increase (Fig. 4c) in the lag properties for cumulative bands as it is showing a macroscopic view. In order to show that the nature is not exactly same for each individual bands, we

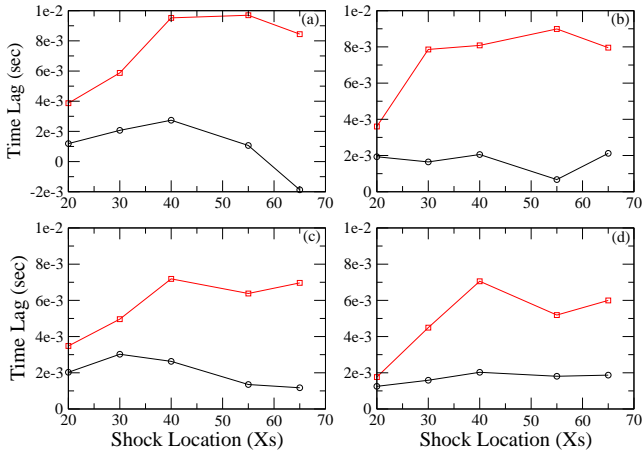


Figure 8. Time lags of 5 – 7 keV (solid-black-circle) and 25 – 30 keV (solid-red-triangle) photons with respect to soft band 2 – 5 keV is plotted for 10°, 36°, 60° & 80° in panels (a), (b), (c) &

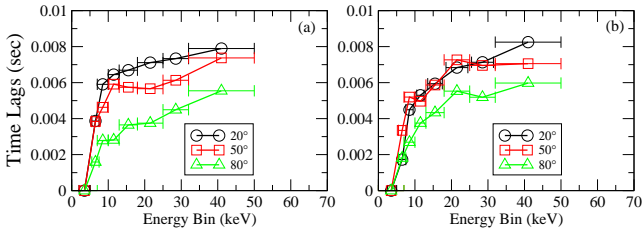


Figure 9. Time lag w.r.t 2 – 5 keV is plotted with energy bins for shock locations at (a) $30r_g$ (a) and (b) $55r_g$ for three different inclination angles. For both Compton cloud sizes, lag magnitude decreases with inclination angle.

have plotted Fig. 8. Non-monotonicity of the lag in Fig. 8 could be attributed to the non-monotonicity of temperature or density inside the CENBOL.

For high inclination angle sources, the gravitational lensing and disk reflection play major role. This is the reason for smooth increase of lag with shock location for high inclination angle sources presented in the panel (c) of Fig. 4. Panel (b) represents the medium inclination angle sources. Neither lensing nor the reflection mechanism dominates for this case. So, this is a region of combination of three contributions, namely, Comptonization, disk reflection and lensing. This is reflected in the nature of the curves. Another reason is that the temperature and density inside the CENBOL is not monotonic, being highest at the centre of the disk. Thus, emerging photons of various energies see different optical depths when inclination angle changes.

Panel 4(a) shows the variation for the case with very low inclination angle where focusing is much stronger than the disk reflection component. Curved geodesics are focussed in axial direction due to the strong gravity of black hole. Here, we can see t_{lag} increases with shock location. But, after a certain CENBOL size it starts to decrease. For Keplerian disk also, the inner region photons come earlier than that of the outer region as shown in Fig 7a when the view is ‘pole on’. But, in presence of Comptonization, for smaller CENBOL size, the Comptonization time compensates the arrival lead of hard photons from the inner regions. But,

when CENBOL size grows bigger, the relatively harder photons scattered from the top region of CENBOL will surely reach the observer before the photons from Keplerian disk as the inner edge of Keplerian disk is far away from the line of sight of the observer. This makes the change in slope shown in Fig. 4a. Such an effect is only visible when the CENBOL is big. The light travel time increases the time delay between the near and far side of the Keplerian disk with increasing inclination angle. But, the secondary photons and the photons from inner regions remain almost at the similar time of arrival region for medium and high inclination angle cases (compare Fig. 7(b) and 7(c)). This variation of time of arrival delay between the photons originated from two sides causes smooth increase of time lag in Fig. 4c.

In Fig. 9, we plot the time lag variation with energy for different inclination angles for a fixed CENBOL size: (a) for $30r_g$ and (b) for $55r_g$. For the same accretion disk geometry, the magnitude of time lag decreases with increasing inclination angle. From Fig. 7, it is clear that an accretion disk of diameter $60r_g$ would cause $60r_g/c$ time delay due to light crossing. So, in this current context, the diameter being $200r_g$, this would cause $200r_g/c$ ($0.02s$ or even more if secondary photons and disk reflection are considered) delay of arrival of the photons from the other side of the Keplerian disk. But, this contribution will reduce the time lag due to Comptonization if a maximum number of photons (for higher optical depth of the cloud) from the other side is intercepted by the CENBOL region. Thus, the lag magnitude decreases with inclination angle and the difference of time lag values (Fig. 9) for high and low inclination angle of a given CENBOL size are in agreement.

In CCG17, the appearance of the Keplerian disk through the Compton cloud is shown for particular optical depth cases. When photons from the far side of the Keplerian disk gravitationally bend and pass through the CENBOL to reach the observer, the travel time of soft photons increases. Since the time of the reference band has increased significantly by gravitational bending the relative lag between two bands or lag magnitude has decreased for higher inclination angles. Due to bending of light, it is possible to find negative lag for high inclination angle sources for a critical shock location X_c and optical depth (see DC16 for further discussion). This happens when the shock strength is increased. These cases will be explored elsewhere.

6 COMPARISON WITH OBSERVATIONAL RESULTS

Nowak et al. (1999), showed that the time lag decreases with Fourier frequency obtained for various energy bands. The energy dependent time lag of Cyg X-1 also shows that the harder photons arrive late. Altamirano & Mendez, 2015, reported the variation of phase lag of GX 339-4 and Cyg X-1 with intensity. The study of time/phase lag is given importance since it provides the information about the accretion flow dynamics. Similar behavior of time lags were also reported for Supermassive Black Holes (see Kara et al. 2013 for details). Recently, DC16, found the correlation between time lag and QPO centroid frequency for outbursting candidates such as XTE J1550-564 and GX 339-4 where they have shown the magnitude of time lag is inversely propor-

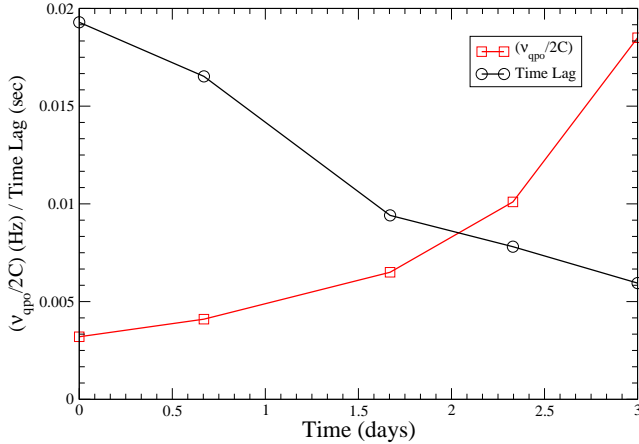


Figure 10. Time lag between 5 – 100 and 0.1 – 5 keV (solid-black-circle) photons is plotted for 50° inclination angle along with calculated $\nu_{qpo}/2C$ Hz (solid-red-triangle). X-axis represents the day of evolution.

tional to the QPO frequencies. These basic natures of time lag are reported in literature. Here, in this section, we show the simulated results of correlation between QPO frequencies and time lags as obtained using TCAF solution.

According to CM00, the shock location is inversely related to the QPO: larger the CENBOL size or shock location, smaller is the value of QPO centroid frequency. We consider the biggest ($65r_g$) CENBOL size is the first occurrence. In an outburst source, it shrinks day by day to produce softer spectra. The evolution mechanism can be found in details in Debnath et al. (2014); Mondal et al. (2014); Molla et al. (2016); Jana et al. (2016); & Chatterjee et al. (2016). We assume the shock is moving inwards with a constant velocity of 500 cm/s. The value of shock velocity is of the same order with that of the results obtained by Molla et al. (2016).

For a fixed inclination angle (50°), we plot the time lag variation with the day along with $(\nu_{qpo}/2C)$ where C is a constant (CM00). From Fig. 6, we see that the time lag is maximum for lowest QPO occurrence and it slowly decreases with increasing QPO frequency. This result is in complete agreement with the Fig. 4 of DC16 where they showed a similar variation for GX 339-4. Inclination angle of this source is reported as ($\sim 50^\circ$) (Zdziarski et al. 1998).

7 DISCUSSIONS AND CONCLUSION

From our simulations, we clearly see the time lag varies with the size of the CENBOL, acting here as the Compton cloud. The lag variation with energy of photons is also clearly present in both observation and our simulation. Explicit dependence of time lag with inclination angle can be understood from our work. For very low inclination objects, we have simulated results which shows soft lags for (5 – 7) keV and (7 – 10) keV energy bins. We speculate that this lag will be there for Hard and Hard Intermediate states where the CENBOL size is big enough.

For high inclination angles, sources tend to have more hard photons since there is paucity of photons from the standard disk. Earlier in the RXTE era, the energy de-

pendent study of lag was limited up to 25 keV. Recently, ASTROSAT provided the data to study lag up to 50 keV (e.g., Jadav et al 2016; Mishra et al. 2016). Observationally, soft lags are mostly found for the high inclination angle sources such as, XTE J1550-564, GRS 1915+105, H1743-322, MAXI J1543-564 and XTE J1859+226 (see, DC16; Yadav et al. 2016; Mishra et al. 2017 and Eijnden et al. 2017 for details). In our picture, this effect is due to the down-scattering of outgoing photons at the regions immediately inside the CENBOL when the shock strength is high, especially near the equatorial plane. In a time independent model of CENBOL (following C85), this is not possible to show unless we carry out time dependent fluid dynamics results coupled with Monte-Carlo simulation which is very time consuming. The behavior of CENBOL in time dependent simulations are different than the thick disk geometry (for details see Molteni, Lanzafame, & Chakrabarti, 1994 (MLC94); Ryu, Chakrabarti, & Molteni, 1997 (RCM97), Giri & Chakrabarti et al. 2010; Giri & Chakrabarti 2012; Giri, Garain & Chakrabarti 2015). The electron density inside Compton cloud is sharply high at the outer edge due to shock compression. The advection component opens up the cusp region and outflows are present in time evolution. Photons could suffer down-scattering at the post-shock region and this increases the soft photon travel time. Soft lags are mostly found for cases where the QPO frequencies are relatively higher and the system is mostly in Hard Intermediate State (HIS). In this state, the system is expected to have jet activity. The signature of jets for XTE J1550-564 in its 1998 outburst has been reported in Wu et al. (2002). The lag behavior started to change the sign on MJD 51073 and the jet activity is increased rapidly at that time. So, the inclusion of jets and time dependent features of Compton cloud is expected to improve the results further. In this paper, our motto is to discuss the origin of time lag behavior with a very simplified TCAF solution. However, even with this simplified model, we obtain a behavior similar to the observational results (Fig. 10). Time dependent aspects of time lag behavior and its evolution with the spectral states are beyond the scope of the present paper and will be discussed elsewhere.

8 ACKNOWLEDGEMENTS

The work of AC is supported by Ministry of Earth Science (MoES), India.

REFERENCES

- Abramowicz M. A., Jaroszynski, M. & Sikora M., 1978, A&A, 63, 221
- Altamirano D. & Mndez M., 2015, MNRAS, 449, 4027
- Chakrabarti S. K., 1990, MNRAS, 245, 747
- Chakrabarti S. K. & Manickam, S., 2000, ApJ, 531, 41
- Chakrabarti S. K., 1985, ApJ, 288, 1, (Paper 1)
- Chakrabarti S. K., 1985, ApJ, 288, 7, (Paper 2)
- Chakrabarti S. K., 2002, Accretion Process on a Black Hole, Allied Publishers
- Chakrabarti S. K. & Das, S. 2004, MNRAS, 349, 649
- Chakrabarti S. K. 1990b, MNRAS, 243, 610
- Chakrabarti S. K., 1996, ApJ, 464, 664(C96)

- Chakrabarti S. K. & Titarchuk L. G., 1995, *ApJ*, 455, 623
- Chatterjee A. & Chakrabarti S. K., 2015, *ASInC*, 12, 95C
- Chatterjee A. & Chakrabarti S. K., 2015, Submitted for 14th Marcel Grossmann proceedings, World Scientific, arXiv:1611.06484v1
- Chatterjee A., Chakrabarti S. K. & Ghosh H., 2017, *MNRAS*, 465, 3902
- Chatterjee D., Debnath D., Chakrabarti S. K., Mondal S. & Jana A., 2016, *ApJ*
- Cui W., Chen W., & Zhang S. N., 1999, *ApJ*, 484, 383
- Cui W., Zhang S. N., Chen W., 2000, *ApJL*, 531, L45
- Debnath D., Mondal S., Chakrabarti S. K., 2014, *MNRAS*, 440, 121
- Debnath D., Mondal S., Chakrabarti S. K., 2015, *MNRAS*, 447, 1984
- Dutta B. G., Chakrabarti S. K., 2016, *ApJ*, 828, 101
- Garain S. K., Ghosh H., Chakrabarti S. K., 2012, *ApJ*, 758, 114
- Garain S. K., Ghosh H., Chakrabarti S. K., 2014, *MNRAS*, 437, 1329
- Giri K., Chakrabarti S. K., Samanta M. M. & Ryu D., 2010, *MNRAS*, 403, 516
- Giri K., & Chakrabarti, S. K., 2012, *MNRAS*, 421, 666
- Giri K., Garain S. K. & Chakrabarti S. K., 2015, *MNRAS*, 448, 3221
- Ghosh H., Garain S. K., Giri K., Chakrabarti S. K. 2011, *MNRAS*, 416, 959G
- Ghosh H., Chakrabarti S. K., Laurent P., *IJMPD*, 18, 2009, 1693
- Ghosh H., Garain S. K., Chakrabarti S. K., Laurent P., 2010, *IJMPD*, 19, 607
- Haardt F., & Maraschi L., 1991, *ApJ*, 380, 51
- Haardt F., & Maraschi L., 1993, *ApJ*, 413, 507
- Heil L. M., Uttley P., Klein-Wolt M., 2015, *MNRAS*, 448, 3348
- Jana A., Debnath D., Chakrabarti S. K., Mondal S., Molla A., A., 2016, *ApJ*, 819, 107
- Kozłowski M., Jaroszynski, M., Abramowicz M. A., Jaroszynski, M., 1978, *A&A*, 63, 209
- Kara E., Fabian A. C., Cackett E. M., Uttley P., Wilkins D. R. & Zoghbi A., 2013, *MNRAS*, 434, 1129
- Landau L. D. & Lifshitz E. D., *Fluid Mechanics*, 1959, Pergamon, New York
- Laurent P., Titarchuk L. G., 1999, *ApJ*, 511, 289
- Maraschi L., Roasio R. & Treves A., 1982, *ApJ*, 253, 312
- Misra R. et al., 2017, *ApJ*, 835, 195
- Miyamoto S., Kitamoto S., Mitsuda K., Dotani, T., 1988, *Nature*, 336, 450
- Molla A. A., Debnath D., Mondal S., Chakrabarti S. K., Jana, A., 2016, *ApJ*, 460, 3163
- Molteni, D., Lanzafame, G., & Chakrabarti, S. K. 1994, *ApJ*, 425, 161
- Molteni, D., Sponholz, H., & Chakrabarti, S. K. 1996, *ApJ*, 457, 805
- Nowak M. A., Wilms J., Dove J. B., 1999, *ApJ*, 517, 355
- Ohkawa Y., Kitamoto S., Kohmura T., 2005, *ApJ*, 621, 951
- Paczysky B., Wiita P. J., 1980, *A&A*, 88, 23
- Page D. N., Thorne K. S., 1974, *Astrophys. J.*, 191, 499
- Payne D. G. 1980, *ApJ*, 237, 951
- Poutanen J., Fabian A. C. 1999, *MNRAS*, 306, L31
- Pozdnyakov A., Sobol I. M., Sunyaev R. A., 1983, *Astrophys. Space Sci. Rev.*, 2, 189
- Qu, J. L., Lu, F. J., Lu, Y., et al. 2010, *ApJ*, 710, 836
- Rees M. J., Begelman M. C., Blandford R. D., Phinney, E. S., 1982, *Nature*, 295, 17
- Ryu, D., Chakrabarti, S. K., & Molteni, D., 1997, *ApJ*, 474, 378
- Sunyaev R. A. & Titarchuk L. G., 1989, *A&A*, 86, 121
- Takahara F., Tsuruta S. & Ichimaru S., 1981, *ApJ*, 251, 26
- Uttley, P., Wilkinson, T., Cassatella, P., et al. 2011, *MNRAS*, 414L, 60
- van den Eijnden, J., Ingram, A., Uttley, P., Motta, S. E., Belloni, T. M., Gardenier D. W., 2017, *MNRAS*, 464, 2643
- Wu K., Soria, R. et al., 2002, *ApJ*, 565, 1161
- Yadav J. S. et al., 2016, *ApJ*, 833, 27
- Zdziarski, A. A., Poutanen, J., Mikolajewska, J., et al. 1998, *MNRAS*, 301, 435